Chapter 5

Elongation and Toughness Models

The most common experiments done on weld metals include the testing of a sample in tension to measure the strength and ductility, and the measurement of the Charpy impact toughness. Although these tests are quite simple to conduct, the principles governing the properties that are measured are understood only on a qualitative basis. In the previous chapter, neural network models which allow the estimation of the yield and ultimate tensile strengths of ferritic steel weld metals using a vast quantity of data collected from the published literature and from commercial sources were developed. The predictions that can be made using these models are associated with error bars which consist of the perceived level of noise in the output and a component representing the uncertainty of fitting. The predictions are reliable when the error bars are small, but have to be used with caution when they are not; large error bars can indicate a need for further experiments to fill gaps in knowledge. In this sense, all predictions are useful irrespective of the magnitudes of the error bars.

The purpose of the work presented here was to develop similar models for the elongation and Charpy properties. There has been little practical progress in modelling the tensile ductility of weld metals [91]. The ductility can to a good approximation be divided into two components whose magnitudes are assumed to be controlled by different physical processes. These components are the uniform plastic strain, as recorded prior to the onset of necking in the tensile specimen, and the non–uniform component which is the remainder of the plastic strain.

By factorising the ductility in this way, it is possible to express the nonuniform component in terms of the inclusion content of the weld deposit, after taking into account variations in specimen cross–sectional area A_O and gauge length L_O [92]:

$$\text{nonuniform elongation}, \% = 100 \times \beta \frac{A_0^{0.5}}{L_0} \tag{5.1}$$

where β is Barba's constant, but now expressed as a function of the inclusion content [93]:

$$\beta \simeq 1.239 - 9.372 \times (\text{wt.\%O}) + (\text{wt.\%S}) \tag{5.2}$$

There is as yet no reliable model for estimating the uniform component of strain, but such a model would require a detailed knowledge of the strain hardening behaviour of the individual phases of the microstructure, together with some theory for multiphase deformation. As far as the nonuniform component is concerned, equation 5.1 emphasises the role of particles in reducing ductility. There are only two inputs to equation 5.2, whereas a vast number of other variables are known to influence the elongation that is measured in a tensile test. Hence the need for a different approach which encompasses a wider set of variables.

The concept of toughness as a measure of the energy absorbed during fracture is well–developed [18, 94]. It is often measured using notched–bar impact tests of which the most common is the Charpy test. A square section notched bar is fractured under specified conditions and the energy absorbed during fracture is taken as a measure of toughness. The Charpy test is empirical in that the data cannot be used directly in engineering design. It does not provide the most searching mechanical conditions. The sample has a notch, but this is less sharp than an atomically sharp brittle crack. Although the test involves impact loading, there is a requirement to start a brittle crack from rest at the tip of the notch, suggesting that the test is optimistic in its comparison against a propagating brittle crack [94]. Most materials can be assumed to contain sub–critical defects so that the initiation of a crack seems seldom to be an issue.

The Charpy test is nevertheless a vital quality control measure which is specified widely in international standards, and in the ranking of samples in research and development exercises. It is the most common first assessment of toughness and in this sense has a proven record of reliability. The test is usually carried out at a variety of temperatures in order to characterise the ductile–brittle transition intrinsic to body–centered cubic metals with their large Peierls barriers to dislocation motion.

It would therefore be useful to be able to quantitatively model the Charpy toughness as a function of metallurgical variables that are believed to influence the cleavage and ductile fracture modes of commercial steels. Some of these variables have in the past been studied quantitatively (for example, the flow stress as a function of temperature [25]) whereas others (such as the degree of organization in the microstructure [5]) have been expressed using language alone.

Complex problems such as those described above, can usefully be modelled empirically using an artificial neural network. The method has been discussed thoroughly in Chapter 3.

5.1 Elongation Model

This model consists of the 20 input variables listed in Table 5.1, which are considered to influence ductility. The detailed chemical composition, the heat treatment and the welding heat input and interpass temperature essentially determine the microstructure and properties. It is easy to imagine other variables which might be important, such as the size distribution of

oxide particles. However, the compilation of a dataset for neural network analysis is always a compromise between two factors. Firstly, a larger dataset is of value in creating a model based on a greater span of knowledge. However, the probability of finding appropriate data diminishes as the number of variables is increased, because incomplete sets of inputs can not be used in the analysis. The database reflects multipass welds made using the submerged arc, gas tungsten arc and manual metal arc welding processes. The welding parameters are represented by the heat input and the interpass temperature; the post–weld heat treatment conditions are represented by temperature and time. The sources of the data are listed in references [29] to [105]. The elongation values are those measured on standard, cylindrical tensile test specimens, where the gauge length is generally specified to be $5.65\times\sqrt{A}$, where A is the cross–sectional area.

Input element	**Minimum**	**Maximum**	**Mean**	**Standard deviation**
Carbon (wt%)	0.01	0.16	0.07	0.0184
Silicon (wt%)	0.01	1.14	0.35	0.124
Manganese (wt%)	0.24	2.31	1.23	0.386
Sulphur (wt%)	0.002	0.14	0.008	0.005
Phosphorus (wt%)	0.001	0.25	0.01	0.007
Nickel (wt%)	0.0	5.48	0.322	0.88
Chromium (wt%)	0.0	9.4	0.45	1.19
Molybdenum (wt%)	0.0	2.4	0.17	0.358
Vanadium (wt%)	0.0	0.32	0.015	0.044
Copper (wt%)	0.0	2.04	0.063	0.204
Cobalt (wt%)	0.0	2.8	0.005	0.097
Tungsten (wt%)	0.0	3.86	0.024	0.207
Oxygen (p.p.m.)	63.0	1650	414	118
Titanium (p.p.m.)	0.0	1000	86	127
Boron (p.p.m.)	0.0	200	11	30
Niobium (p.p.m.)	0.0	1770	48	141
Heat input (kJ mm^{-1})	0.55	4.8	1.23	0.71
Interpass temperature (°C)	20	350	204	35
Tempering temperature (°C)	20	750	321	191
Tempering time (h)	0.0	32	10	6.2
Elongation (%)	7.4	41.1	26	5

Table 5.1: The variables used in developing the elongation model. 'p.p.m.' corresponds to parts per million by weight.

A total of 1972 individual experimental data were gathered. In 19 cases, the sulphur and phosphorus concentrations were not reported, in which case they were set to the average values of the other data in the database. This is a better procedure than setting the concentrations to zero because all welds inevitably contain impurities. On the other hand, alloying additions such as molybdenum can be set to zero when they are not added deliberately, without affecting

the overall microstructure or mechanical property outcomes. A visual impression of the whole elongation database is shown in Fig. 5.1. The mean and standard deviation of the percentage elongation are 26 and 5 respectively, showing that most of the data lie in the range 21-31%, Fig. 5.2.

The training, test and log predictive errors [6] associated with each of the eighty models created are shown in Fig. 5.3. The behaviour of the single best model is illustrated in Fig. 5.3d,e. From the set of 80 models, a committee of 58 of the best models was found to give the lowest test error, Fig. 5.3c; each member of the committee was then retrained on the entire dataset to create the final committee model Fig. 5.3f). The details of all these procedures are described in Chapter 3. Fig. 5.4 shows the significance σ_w of each of the input variables. The behaviour of the committee model in making predictions for specific cases is now illustrated for C–Mn weld metals.

5.1.1 Application to C–Mn Weld Metals

The set of variables used for analysis is listed in Table 5.2; any variations illustrated in subsequent diagrams are about these values. An increase in the strength is expected to lead to a decrease in elongation [106]. It is not surprising, therefore, that the elongation decreases when the manganese and carbon concentrations are increased, Fig. 5.5. Notice also that the effect is more pronounced at higher manganese concentrations, consistent with the corresponding effect on strength (Chapter 4).

Ductile fracture can be described in terms of the nucleation, growth and coalescence of voids. Macroscopic fracture occurs when the voids link on a large enough scale. If the number density of voids is large, then their mean separation is reduced and coalescence occurs rapidly, giving a minimal amount of plastic deformation before fracture, and reducing the overall ductility (Fig. 5.6).

It has generally been assumed that in weld metals both sulphur and oxygen contribute to the inclusion content and hence must be detrimental to the toughness. Whereas it is found that an increase in the oxygen concentration definitely reduces the elongation (Fig. 5.7a), the picture for sulphur is not clear. The data in fact show a slight increase in elongation with the sulphur concentration but the trend is not meaningful when the error bars are taken into account (Fig. 5.7b). Oxides are the main inclusions in weld metals [90] whereas sulphur tends to be deposited in the form of very thin layers on top of the oxide particles [107]. The observed trends may not therefore be unreasonable in weld metals as opposed to wrought steels which tend to have a very low oxygen concentration with a predominance of sulphide inclusions.

Another interesting feature of the difference between weld metals and C–Mn type hot–rolled steels is revealed by comparing the dataset used in a previous analysis for wrought alloys [108]

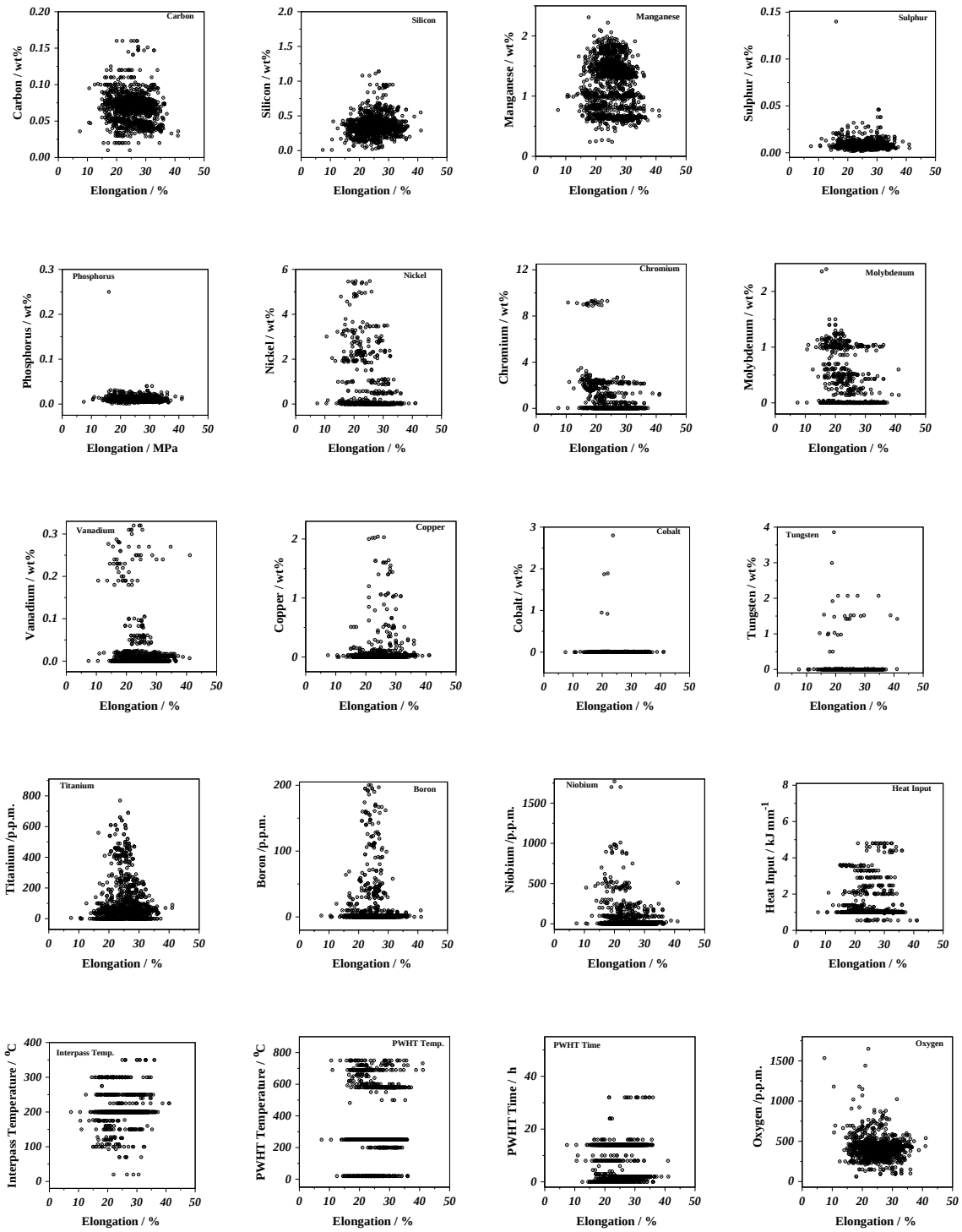

Figure 5.1: The database values of each variable versus the elongation. 'p.p.m.' refers to parts per million by weight.

with the present work which is on weld metals (Fig. 5.8). The difference between the yield strength (σ_{YS}) and ultimate tensile strength (σ_{UTS}) for welds is approximately constant at

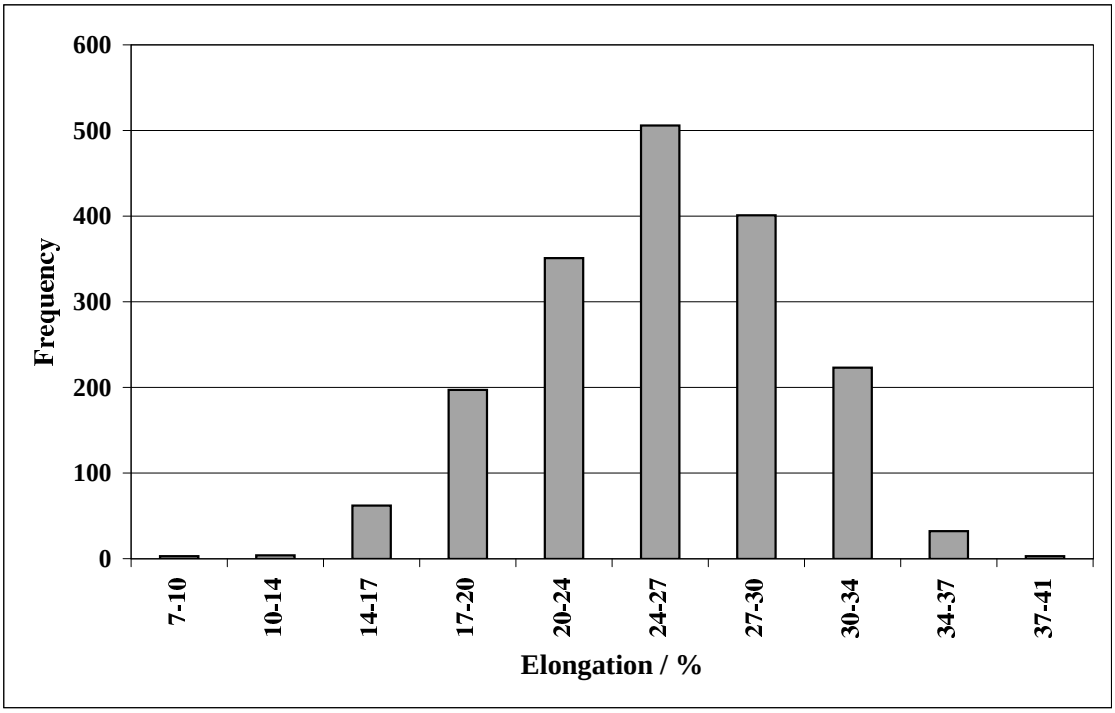

Figure 5.2: The elongation data frequency distribution.

100 MPa whereas for plates, the difference becomes smaller as the strength increases. The stress can be described as a function of plastic strain ε using a power law of the form

$$\sigma = K\varepsilon^n \tag{5.3}$$

where K and n are constants, the latter being the strain hardening coefficient. Since the yield strength is measured at a plastic strain of 0.02, and the UTS is given by Kn^n, it follows that

$$\sigma_{UTS} - \sigma_{YS} = K[n^n - 0.02^n] \tag{5.4}$$

Since for the welds, $\sigma_{UTS} - \sigma_{YS} \simeq 100\,\text{MPa}$, it follows that the strain hardening coefficient must be approximately constant for all the welds considered. This in turn means that the uniform strain component of the measured elongation of most ferritic steel welds must be about constant, the total elongation being a function mostly of the non–uniform component which occurs beyond necking during a tension test. Of course, the non–uniform component of the elongation depends largely on void nucleation, growth and coalescence so it is not surprising that the total elongation depends strongly on inclusions.

We note that this interpretation does not explain why the strain hardening coefficient for

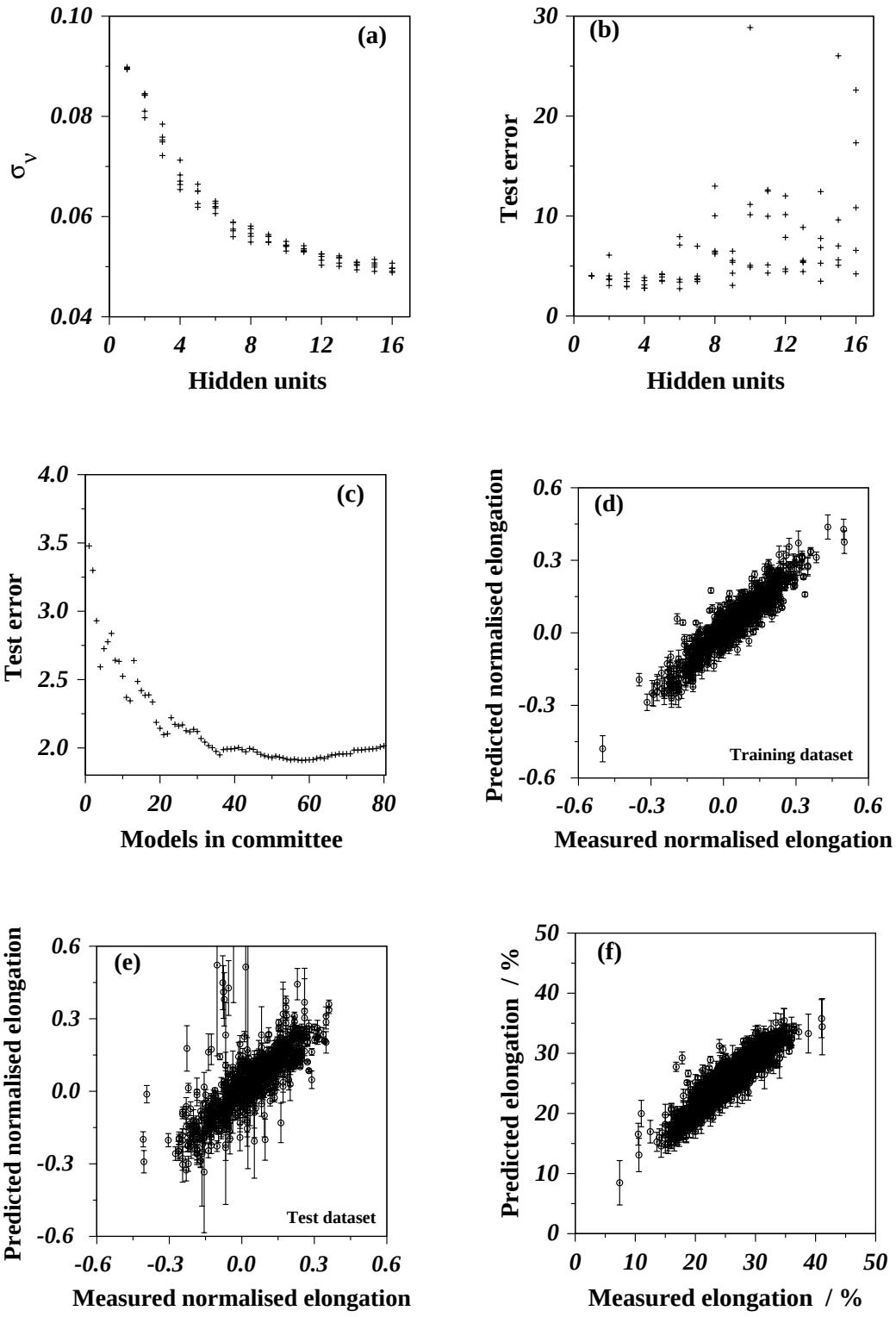

Figure 5.3: Characteristics of the elongation model. σ_ν is the model perceived level of noise in the elongation. (d) and (e) represent the behaviour of the best single model, whereas (f) shows the performance of the optimum committee model on the entire dataset.

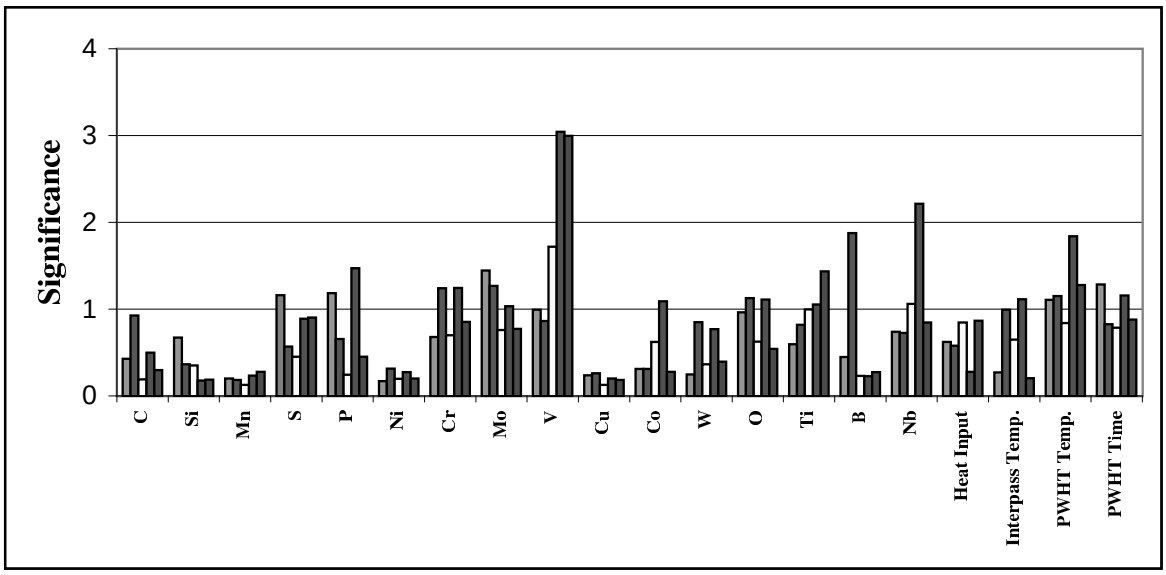

Figure 5.4: The perceived significance σ_w of each of the input variables, as perceived by first best five neural network models in committee, in influencing the elongation.

welds is approximately constant whereas that of plates is not. This remains an issue for further work.

A further consequence of these observations is that the ratio of the yield to ultimate tensile strength will increase more rapidly for welds than for plates, which may in turn have consequences on the fatigue properties. The fatigue resistance is generally higher for materials where there is a large difference between the yield and ultimate tensile strength. Indeed, Fig. 5.9 shows that unlike plate steels, there is not much that can be done to control the ratio σ_{YS}/σ_{UTS} by alloying.

5.2 Charpy Toughness Model

This model was developed with 22 input variables, Table 5.3, the nitrogen concentration and the test temperature being the additional variables when compared with the elongation model (Fig. 5.10). The test temperature is expected to be an important variable because of the ductile–brittle transition in ferritic iron, and the nitrogen concentration is known to have an influence via strain hardening effects. Unfortunately, the Charpy data that are available are not uniformly distributed (Fig. 5.11) because the tests are frequently reported in literature at specified Charpy toughness values.

Input variable	
Carbon (wt%)	0.06
Silicon (wt%)	0.50
Manganese (wt%)	1.50
Sulphur (wt%)	0.006
Phosphorus (wt%)	0.008
Nickel (wt%)	0.0
Chromium (wt%)	0.0
Molybdenum (wt%)	0.0
Vanadium (wt%)	0.0
Copper (wt%)	0.0
Cobalt (wt%)	0.0
Tungsten (wt%)	0.0
Oxygen (p.p.m.)	300
Titanium (p.p.m.)	0.0
Boron (p.p.m.)	0.0
Niobium (p.p.m.)	0.0
Heat input (kJ mm^{-1})	1.00
Interpass temperature (°C)	175
Tempering temperature (°C)	250
Tempering time (h)	14.0

Table 5.2: The input variables of carbon–manganese steel weld metal used in the analysis.

The models were created from a dataset containing 3142 individual experiments and the results are shown in Fig. 5.12. An optimum committee consisting of around 62 of the best models was used in all subsequent analyses.

5.2.1 Application to C–Mn Welds

The reference values of the variables used in making predictions are listed in Table 5.4. Fig. 5.13 shows the calculated variation in Charpy values for 0 °C as a function of the manganese and carbon concentrations. There are two competing effects:

(i) At first an increase in hardenability leads to a replacement of deleterious phases such as allotriomorphic and Widmanstätten ferrite with the desirable acicular ferrite [90], leading to an increase in toughness. It is for this reason that the peak in toughness occurs at a higher carbon concentration when the manganese concentration is low. For equivalent hardenability, the carbon concentration must be larger when that of manganese is small.

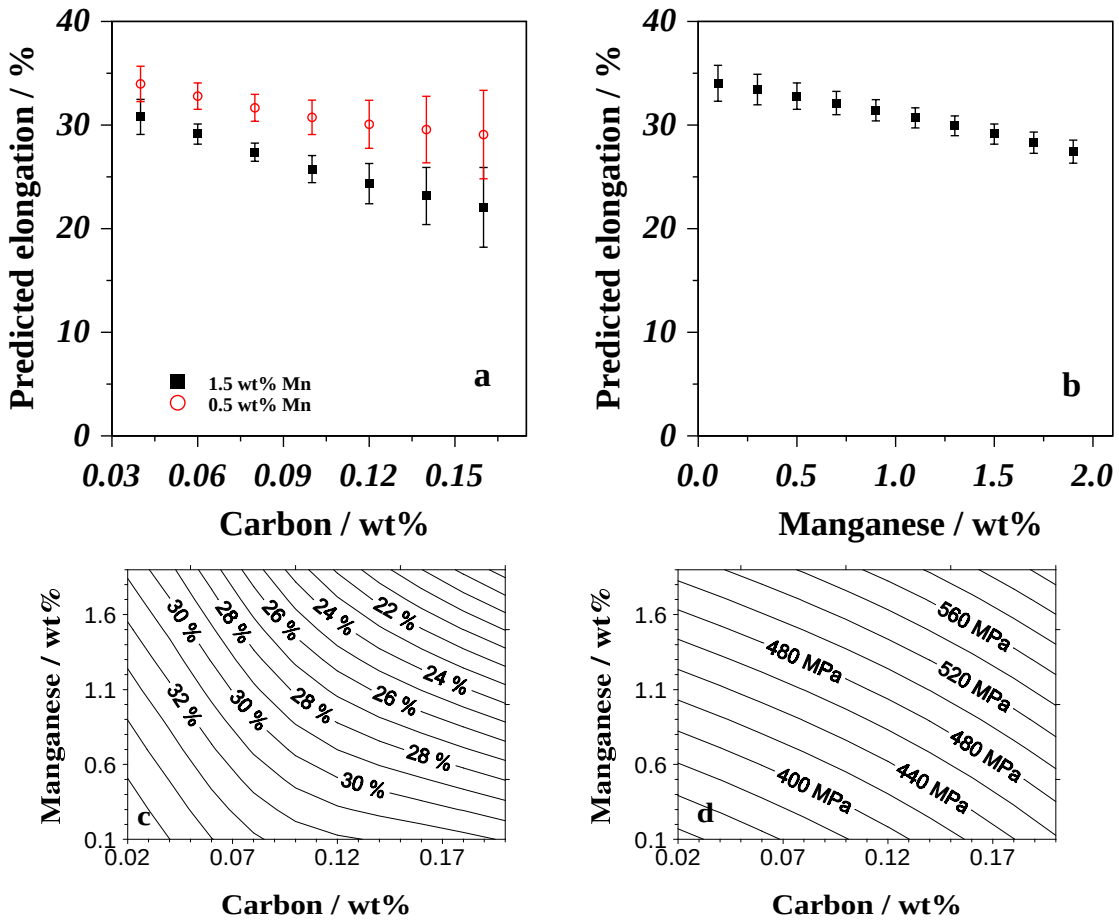

Figure 5.5: (a, b) Predicted elongation as a function of carbon and manganese in carbon–manganese weld metal. (c, d) Contour plots showing the variation in elongation and yield strength as a function of the carbon and manganese concentrations. The error bars have been omitted for clarity but range from ±2–6% in elongation and ±10–30 MPa in the strength plots.

(ii) The strength increases with the Mn and C concentration. In general, an increase in strength leads to a deterioration in toughness because plastic flow becomes more difficult, making cleavage cracking more probable. This increase in strength may also be accompanied by the formation of undesirable phases such as martensite. It follows that the toughness should eventually begin to decrease as the carbon or manganese concentrations are increased.

Both of these effects are well illustrated by the computed data shown in Fig. 5.13. The microstructures for the welds described in Fig. 5.13 were calculated using a published physical model [90]. Fig. 5.14 shows that the above interpretations are correct in that the initial increase in toughness corresponds to an improvement in the microstructure, with the subsequent

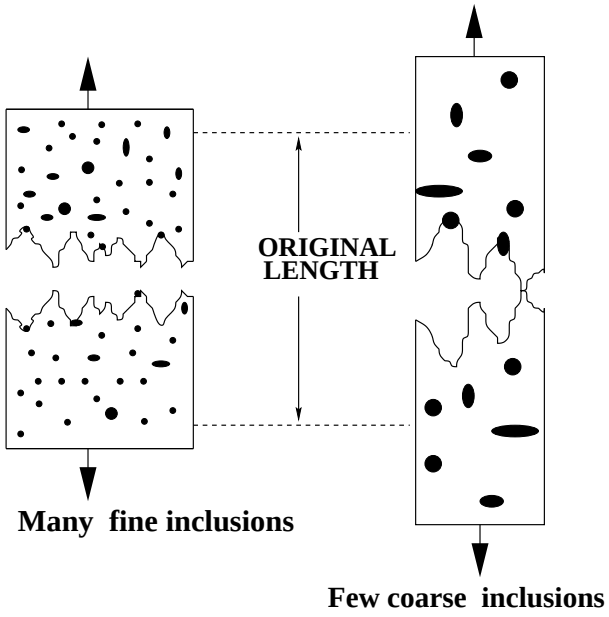

Figure 5.6: An illustration of how a large density of void nucleating particles can result in fracture with a low overall ductility, even though the material fails by gross plastic deformation on a microscopic scale.

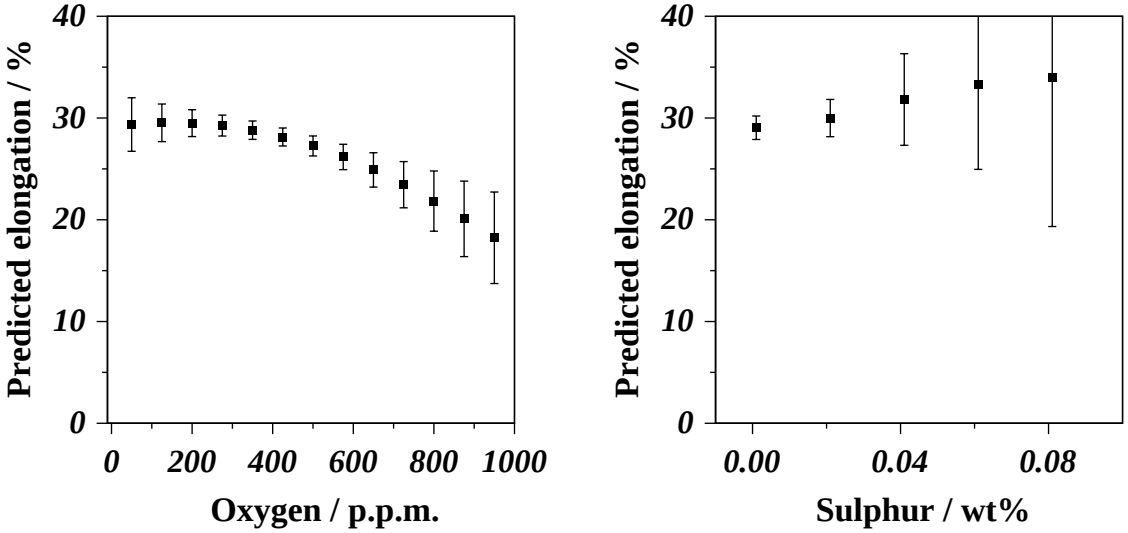

Figure 5.7: Change in elongation in carbon–manganese weld metal as a function of (a) the oxygen concentration and (b) the sulphur concentration. It is evident that sulphur does not have a significant effect on the ductility of welds of the type considered in the present work.

decrease in toughness explained by the increase in strength. The Fig. 5.15 shows clearly that in the context of Charpy impact toughness tests, there is always an optimum combination of manganese and carbon.

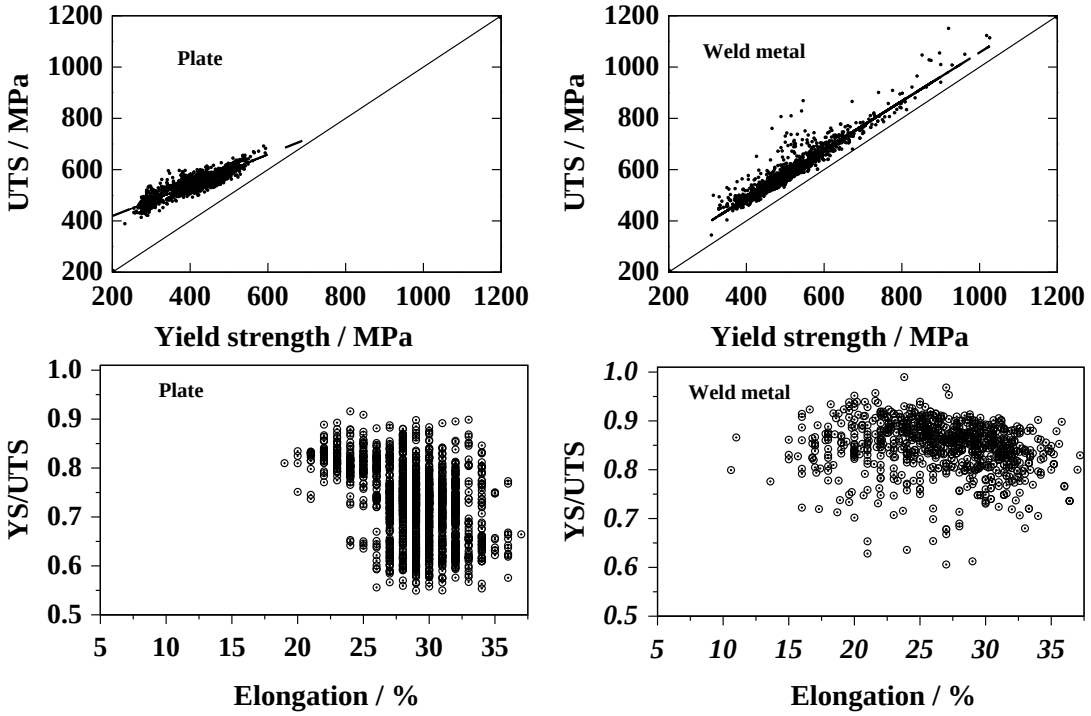

Figure 5.8: Plots of the ultimate tensile strength versus yield strength for (a) hot–rolled C–Mn steel plates; (b) weld metals. Plots of the elongation versus yield strength for (c) hot–rolled C–Mn steel plates; (d) weld metals. All of the data plotted are experiments, those for plates coming from previous work [108], those for the weld deposits from the present analysis.

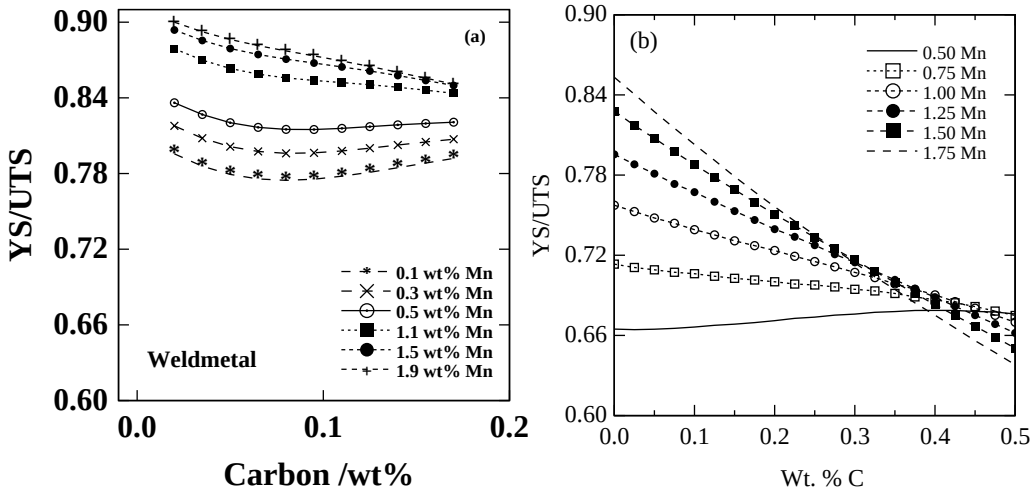

Figure 5.9: The effect of carbon, manganese on YS/UTS ratio on a) weld metal and b) steel plate [108].

Input element	Minimum	Maximum	Mean	Standard deviation
Carbon (wt%)	0.022	0.19	0.07	0.0192
Silicon (wt%)	0.01	1.63	0.36	0.126
Manganese (wt%)	0.23	2.31	1.25	0.403
Sulphur (wt%)	0.002	0.14	0.008	0.008
Phosphorus (wt%)	0.003	0.25	0.01	0.0134
Nickel (wt%)	0.0	5.58	0.366	1.012
Chromium (wt%)	0.0	11.8	0.453	1.387
Molybdenum (wt%)	0.0	1.54	0.153	0.336
Vanadium (wt%)	0.0	0.53	0.0136	0.0424
Copper (wt%)	0.0	2.18	0.0658	0.222
Cobalt (wt%)	0.0	0.016	0.0005	0.0023
Tungsten (wt%)	0.0	3.86	0.0076	0.1555
Oxygen (p.p.m.)	63.0	1535	409	112
Titanium (p.p.m.)	0.0	770	102	138
Nitrogen (p.p.m.)	21.0	1000	96.5	63
Boron (p.p.m.)	0.0	200	14.3	35
Niobium (p.p.m.)	0.0	1770	40.55	139.6
Heat input (kJ mm^{-1})	0.6	6.6	1.194	0.69
Interpass temperature (°C)	20	350	199.7	30
Tempering temperature (°C)	20	760	182.5	261
Tempering time (h)	0.0	100	2.2	5.66
Testing temperature (°C)	-151	136	-43.9	34.4
Charpy toughness (J)	2.6	300	74	43

Table 5.3: The input variables for the Charpy impact toughness model. 'p.p.m'. corresponds to parts per million by weight.

Nickel is known to have an intrinsic beneficial effect on toughness by increasing the work necessary to create cleavage cracks [110]. Thus, the toughness at low temperatures is found to increase with the nickel concentration (Fig. 5.16a); however, the optimum concentration of nickel is found to depend significantly on that of manganese. Higher concentrations of nickel are beneficial only at low concentrations of manganese (Fig. 5.16b) because both elements enhance the hardenability and strength of the weld deposit.

As might be expected, Fig. 5.17a shows that the toughness at 0 °C decreases with an increase in the oxygen concentration; oxides are sites for the nucleation of cracks and voids. The toughness can nevertheless be optimised by selecting the right manganese concentration, 0.7 wt% in the case illustrated. This is because low manganese concentrations lead to bad microstructures whereas too high a concentration raises the weld strength. Fig. 5.17b shows that the toughness is maximised when the manganese to silicon ratio is about 2:1. This may have something to do with deoxidation practice but the details are not understood.

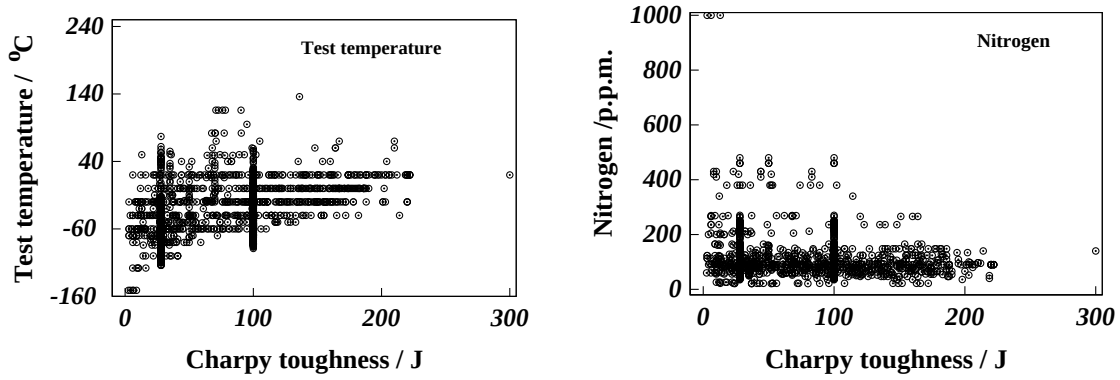

Figure 5.10: The additional variables used in the Charpy toughness model.

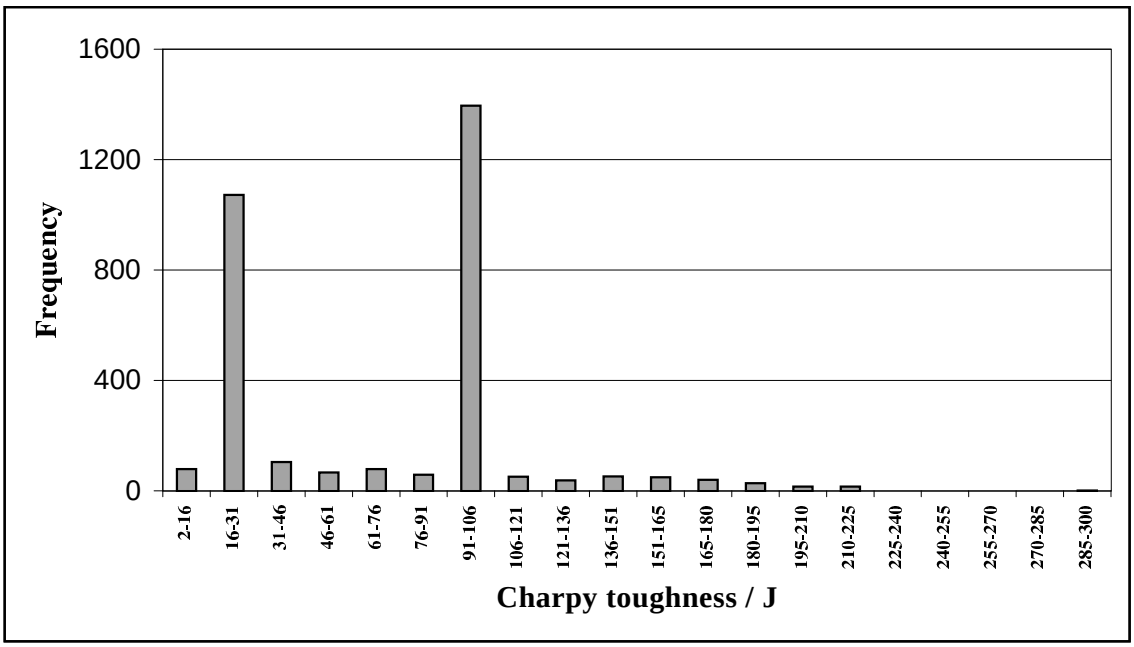

Figure 5.11: Frequency distribution for the Charpy toughness data.

5.2.2 Further Improvements

The analysis presented here is very useful and is the first quantitative model covering a vast range of variables. At the same time the model captures many non–linear dependencies. However, as Fig 5.16 shows the analysis is far from ideal in term of the spread of impact toughness.

To rectify this a more comprehensive set of Charpy results was complied from Evans [54], but these were restricted to carbon–manganese and low–alloy weld metals. The detailed analysis

Input variable	
Carbon (wt%)	0.07
Silicon (wt%)	0.50
Manganese (wt%)	1.50
Sulphur (wt%)	0.006
Phosphorus (wt%)	0.008
Nickel (wt%)	0.0
Chromium (wt%)	0.0
Molybdenum (wt%)	0.0
Vanadium (wt%)	0.0
Copper (wt%)	0.0
Cobalt (wt%)	0.0
Tungsten (wt%)	0.0
Oxygen (p.p.m.)	300
Titanium (p.p.m.)	0.0
Nitrogen (p.p.m.)	80
Boron (p.p.m.)	0.0
Niobium (p.p.m.)	0.0
Heat input (kJ mm^{-1})	1.00
Interpass temperature (°C)	175
Tempering temperature (°C)	20
Tempering time (h)	0.0
Testing temperature (°C)	0.0

Table 5.4: The input variables of carbon–manganese steel weld metal used in the analysis.

of these data is presented in Appendix A. One of the major aims in doing this additional work was to confirm the exciting trend noted in Fig. 5.16. It seems that the widespread belief in industry that nickel additions unconditionally improve low temperature toughness is not entirely justified. Fig. 5.16 confirms that nickel does indeed improve the toughness, but only at low manganese concentrations. Bearing in mind that the importance of this result and the fact that the model from which Fig. 5.16 was generated has a highly non–uniform distribution of data, it is heartening to see that the more comprehensive analysis (Appendix A) confirms the trend, as illustrated in Fig. A.19.

5.3 Impact Energy Transition Temperature Model

As emphasied earlier, the Charpy toughness of a steel weld is one of the important quality control parameters, widely specified in industry and used as a ranking parameter in consumable research

and development programmes. Body–centered cubic iron undergoes a ductile–brittle transition as the test temperature is reduced. Consistent with international norms, the toughness is therefore frequently characterised by a transition temperature corresponding to a particular value of the absorbed impact energy. In a recent paper, French [111] conducted a careful series of experiments in which the temperature T_{27J} corresponding to a measured Charpy impact energy of 27 J was characterised as a function of the yield strength, oxygen content and the microstructure. The latter included the fraction of acicular ferrite in the as–deposited microstructure, but since the work was done on multipass welds, an overall percentage of reheated microstructure was also measured. Three different welding processes were used: flux–cored arc welding (FCAW), gas metal arc welding (GMAW) and manual metal arc welding (MMAW).

The resulting data were analysed using linear regression as follows:

$$T_{27J} = 0.007(YS) + 550(O) + 0.034(R) - 0.31(AF) - 74 \qquad ^{\circ}\mathrm{C} \tag{5.5}$$

where YS is the yield strength in MPa, O is the concentration of oxygen in wt%, and the reheated microstructure R and acicular ferrite AF are area percentages. The range of applicability of the equation can be gauged from Table 5.5, which contains information from 59 separate measurements.

Input element	**Minimum**	**Maximum**	**Mean**	**Standard Deviation**
Yield Strength (MPa)	360	630	516	55
Oxygen (wt%)	0.03	0.12	0.06	0.02
Reheated Material (%)	20	79	41	13
Acicular Ferrite (%)	5	86	54	15
Temperature at 27J (°C)	-88.0	-13	-54	18

Table 5.5: Characteristics of the measured parameters in the experiments conducted by French [111].

The analysis indicated a standard error of $\pm 12\,^{\circ}\mathrm{C}$, with a correlation coefficient of 0.78. It is possible that a better interpretation of the data and associated uncertainties can be obtained using a non–linear regression method, which does not have an *a priori* assumption of the relationship between the variables, which accounts for the interactions between the variables, and which comments not only in the perceived level of noise in the output, but also on how the uncertainty of fitting depends on the particular region of input space where the prediction is being made. The introduction to the method of neural network analysis is presented in Chapter 3.

5.3.1 The Analysis

The aim was to be able to estimate T_{27J} as a function of the variables shown in Table 5.5. All the input variables and the output were normalised within the range ± 0.5 (Chapter 3). This step is not essential to the running of the neural network but later allows a convenient way to compare the results of the output.

For several runs of the neural network, Fig. 5.18 shows the model perceived noise σ_ν in T_{27J}. It is very interesting that the level of noise in the normalised output parameter T_{27J}, as perceived by the network, is $\sim 0.15 - 0.18$. This amounts to $\pm 11 - 14\,^{\circ}$C, which compares favorably with the $\pm 12^{\circ}$C deduced by French using linear regression analysis. It is also worth noting that the error, irrespective of the model, is quite large when considering the physical meaning of T_{27J}. Furthermore, one standard error corresponds to a 68% confidence limit whereas two standard errors give the more acceptable 95% error bound. The important conclusion is that the noise level is not reduced by using a non–linear analysis, giving evidence that the problem is not well specified; there are missing variables which clearly affect the toughness. It cannot be speculated what these missing variables could be, but factors such as the hydrogen and nitrogen concentrations, the scale of the microstructure *etc.* come to mind. Note also that the nature of the welding process is not explicitly taken into account.

A second outcome is that this particular problem illustrates the soundness of the neural network technique used here, where the proper use of the training and test dataset prevents the accidental modelling of true noise in the output.

Fig. 5.19 shows the predictions for the training and test data for the best model, identified as the one with the highest log predictive error [6]. It is clear that the model is reasonably well behaved in the sense that the test data are predicted to a similar level of accuracy as the training data. It is important to note that the error bars plotted in Fig. 5.19a,b do not include σ_ν, but only the fitting error, which depends on the position in the input space. Fig. 5.19c shows the corresponding plot for the test data where the error bars contain both the σ_ν and the fitting error. All subsequent plots also include both components since it is logical to consider both the perceived level of noise in the output and the fitting error. As will be seen subsequently, the latter is particularly important when extrapolating or interpolating, since large fitting errors are calculated in regions where the experimental knowledge is sparse or noisy.

A plot of the test error of the committee versus its size gives a minimum which defines the optimum size of the committee, as shown in Fig. 5.20. The test error associated with the best single model is clearly greater than that of any of the other committees. It was determined in this case that a committee of thirteen models would be the best choice, being the committee of the lowest test error. The committee was then retrained on the entire data set without changing the complexity of any of its members.

The predictions of the committee trained on the entire data set can be compared with the original dataset as shown in Fig. 5.21.

Another parameter, σ_w, indicates the importance of an input in terms of its variation having an effect on the output of the model. Fig. 5.22 compares the values of σ_w for each of the inputs for the thirteen models in committee. A high value of σ_w for a specific input can be caused by the corresponding variable inducing a large variation in the output, but it can be seen from Fig. 5.22 that different models can assign varying significance to the same input. This is one of the reasons why a committee of models can be more reliable than the single model judged to be best on the basis of a parameter such as σ_ν.

5.3.2 Use of the Model

It is worth illustrating a few predictions, to emphasis the point that the error bars will not be constant as in [111]. It is important to note that as in equation 5.5, the predictions are for the case where just one input variable is altered, keeping all other fixed. This may not be possible when conducting experiments. The variables used for analysis are shown in Table 5.6. Fig. 5.23a shows that T_{27J} increases with the oxygen concentration; this is expected since the oxygen is inevitably present in the form of oxide inclusions which, for a constant microstructure, are detrimental to toughness.

Input variable	
Yield Strength (MPa)	515
Oxygen (wt%)	0.05
Reheated Material (%)	41
Acicular Ferrite (%)	54

Table 5.6: The input variables of carbon–manganese steel weld metal used in the analysis.

It is not surprising that Fig. 5.23b shows that acicular ferrite improves the toughness. However, the neural network model shows that the results are not certain at large fractions of acicular ferrite when all the other variables are kept constant.

Fig. 5.24 shows contour plots of T_{27J} as a function of the acicular ferrite and oxygen concentrations. A simple interpretation of the linear regression model (Fig. 5.24b) indicates that for optimum toughness, the acicular ferrite must be maximised at a zero oxygen concentration. However, there are no welds in the dataset with zero oxygen concentration and such a suggestion is probably not justified since oxides are needed to nucleate acicular ferrite. The neural network analysis, on the other hand, correctly indicates an optimum combination of acicular ferrite and oxygen concentration.

5.4 Embrittlement Model

Welding alloys designed for creep–resistant steels frequently have to be tempered in a temperature range where they are susceptible to embrittlement by impurity elements such as antimony or phosphorus. The segregation of these deleterious elements to the prior austenite grain boundaries leads to intergranular failure and consequently, a reduction in toughness. Whereas this mechanism of embrittlement is well–understood from a vast amount of research published over the last five decades, there are no quantitative methods capable of estimating the degree of embrittlement as a function of the chemical composition and heat treatment.

It was in this context that Bruscato [112] reported a large number of experiments, based on the classical $2\frac{1}{4}$Cr1Mo composition, but with variations in the phosphorus, antimony, tin and arsenic concentrations. There were also some variations in the concentrations of the major alloying additions including C, Mn, Si, Cr and Mo. The tendency to embrittlement was monitored by comparing the impact toughness of both post–weld heat treated (PWHT) and step–aged samples. The latter heat treatment exaggerates the extent of embrittlement. Bruscato used an embrittlement factor $\overline{X}$ to interpret his data:

$$\overline{X} = \frac{10\mathrm{P} + 5\mathrm{Sb} + 4\mathrm{Sn} + \mathrm{As}}{100} \tag{5.6}$$

where the concentrations of the elements are in parts per million by weight. A large value of $\overline{X}$ implies a greater tendency to temper embrittlement. This led him to conclude that the embrittlement of $2\frac{1}{4}$Cr1Mo welds is directly related to the manganese, silicon, phosphorus, tin, arsenic and antimony concentrations, with the first four being of greatest significance. The derivation of the equation for $\overline{X}$ was not presented in the original paper, although it is stated that it is based on data from chromium–steels. In the present work Bruscato's original data was analysed using neural network analysis, and his conclusions were examined in more detail.

5.4.1 The Data

Bruscato published results on thirty separate weld deposits; the range of parameters is listed in Table 5.7. The Charpy toughness of the step–aged samples represents the output to be modelled as a function of all the other variables listed in Table 5.7. All of the thirty welds had been given an identical heat treatment. For the purposes of the analysis, the data were all normalised in the range ± 0.5 in order to compare the significance of each of the input variables.

The data were divided at random into two parts, a training and a test dataset. The neural network models were then created using just the training data (Chapter 3). The resulting models were assessed on their ability to generalise on the unseen test data. From the models created, a committee of three models was found to give the best generalisation on unseen data.

Input element	Minimum	Maximum	Mean	Standard Deviation
Silicon (wt%)	0.32	1.19	0.636	0.195
Manganese (wt%)	0.54	0.79	0.691	0.0609
Phosphorus (wt%)	0.004	0.018	0.009	0.003
Molybdenum (wt%)	0.9	1.27	1.102	0.095
Tin (p.p.m.)	70	300	108.7	38.8
Antimony (p.p.m.)	0.9	22	5.2	3.73
Arsenic (p.p.m.)	0.0	130	59.8	27.7
Charpy toughness after step aging (J)	6.78	136.96	60.4	29.2

Table 5.7: The range of values reported by Bruscato, and used in the present work. 'p.p.m.' corresponds to parts per million by weight.

These three models had 13, 11 and 11 hidden units with σ_ν values of 0.083293, 0.083149 and 0.083118 respectively; σ_ν is the perceived level of noise in the normalised output. An increase in the number of hidden units enables the network to recognise more complex relationships. The committee members were finally optimised on the entire dataset. The performance of the committee is illustrated in Fig. 5.25.

Fig. 5.26 shows the significance σ_w of each of the input variables. The value of σ_w for a particular input variable indicates the ability of that input to explain variations in the output (Charpy toughness). Three σ_w values are presented for each input, corresponding to each of the three members of the committee of models. A consistent value of σ_w, for a given input, indicates that there exists a well–defined relationship between that input and the output. Fig. 5.26 shows that tin, antimony and arsenic have very little effect on the embrittlement of the $2\frac{1}{4}$Cr1Mo welds studied, whereas phosphorus has a very large effect.

These observations can be illustrated further by making predictions. Calculations were done using the base set of input values listed in Table 5.8, while varying each input individually.

Input variable	
Silicon (wt%)	0.58
Manganese (wt%)	0.78
Phosphorus (wt%)	0.008
Molybdenum (wt%)	1.05
Tin (p.p.m.)	120
Antimony (p.p.m.)	1.6
Arsenic (p.p.m.)	36

Table 5.8: Base input values used in the application of the embrittlement model. The values correspond to weld Q in [112]. 'p.p.m.' corresponds to parts per million.

Fig. 5.27 shows the effects of molybdenum, silicon, manganese and phosphorus concentrations. As expected, phosphorus has a strong and very significant tendency to embrittle the weld metal; as stated earlier, the mechanism of phosphorus embrittlement is well–understood, involving its segregation to prior austenite grain boundaries. On the other hand, molybdenum actually improves the resistance to embrittlement. This is also expected, because molybdenum and phosphorus atoms tend to associate so that the latter are prevented from segregating to the prior austenite grain surfaces [113].

It is exciting that significant trends are recognised also for manganese and silicon. The manganese effect is consistent with work which suggests that it reduces the intergranular fracture strength [114]. Silicon is known to promote the segregation of phosphorus to the austenite grain boundaries [115].

By contrast, there are no significant trends notable for arsenic, tin or antimony (Fig. 5.28). Based on these observations, we do not find that As, Sn and Sb are important contributors to embrittlement in the particular alloy system studied here. It is possible that this result is a consequence of the fact that the welds all contain phosphorus in concentrations large enough to swamp the much smaller effects of As, Sn and Sb. Thus, the mean phosphorus concentration is 90 p.p.m, with a standard deviation of 30 p.p.m.

5.5 Summary

Tensile elongation and Charpy toughness models have been developed taking into account chemical composition, heat treatment and welding parameters. These models were successfully applied to analyse carbon–manganese weld metals and exciting results were obtained. Theoretically unexplained results were found in few cases of carbon–manganese welds.

It was shown that neural networks does not reduce the large perceived level of noise in the Charpy impact toughness transition temperature (T_{27J}) model. As there are many more variables which control the impact toughness when compared with the restricted set studied in the transition temperature model. The standard error quoted for the linear regression models must be regarded as an underestimate of the real uncertainty, since there will be regions of the input space where the fitting function itself has great uncertainty. This is relevant in both extrapolation and interpolation, which is taken into account by using Bayesian neural networks over other standard regression methods. The transition temperature model, unlike the regression model correctly predicts that there is a combination of acicular ferrite and oxygen which optimises toughness.

With the embrittlement model (Section 5.4) it was found that phosphorus, silicon and manganese all make $2\frac{1}{4}$Cr1Mo welds susceptible to temper embrittlement, with the embrittling potency decreasing in that order. Molybdenum decreases the tendency to impurity induced

embrittlement. These observations are all expected from published work. By contrast, As, Sb and Sn have no perceptible effect on the welding alloys studied, probably because of the overwhelming influence of phosphorus. It follows that any attempt to reduce the effects of temper embrittlement should focus primarily on reduction in the phosphorus.

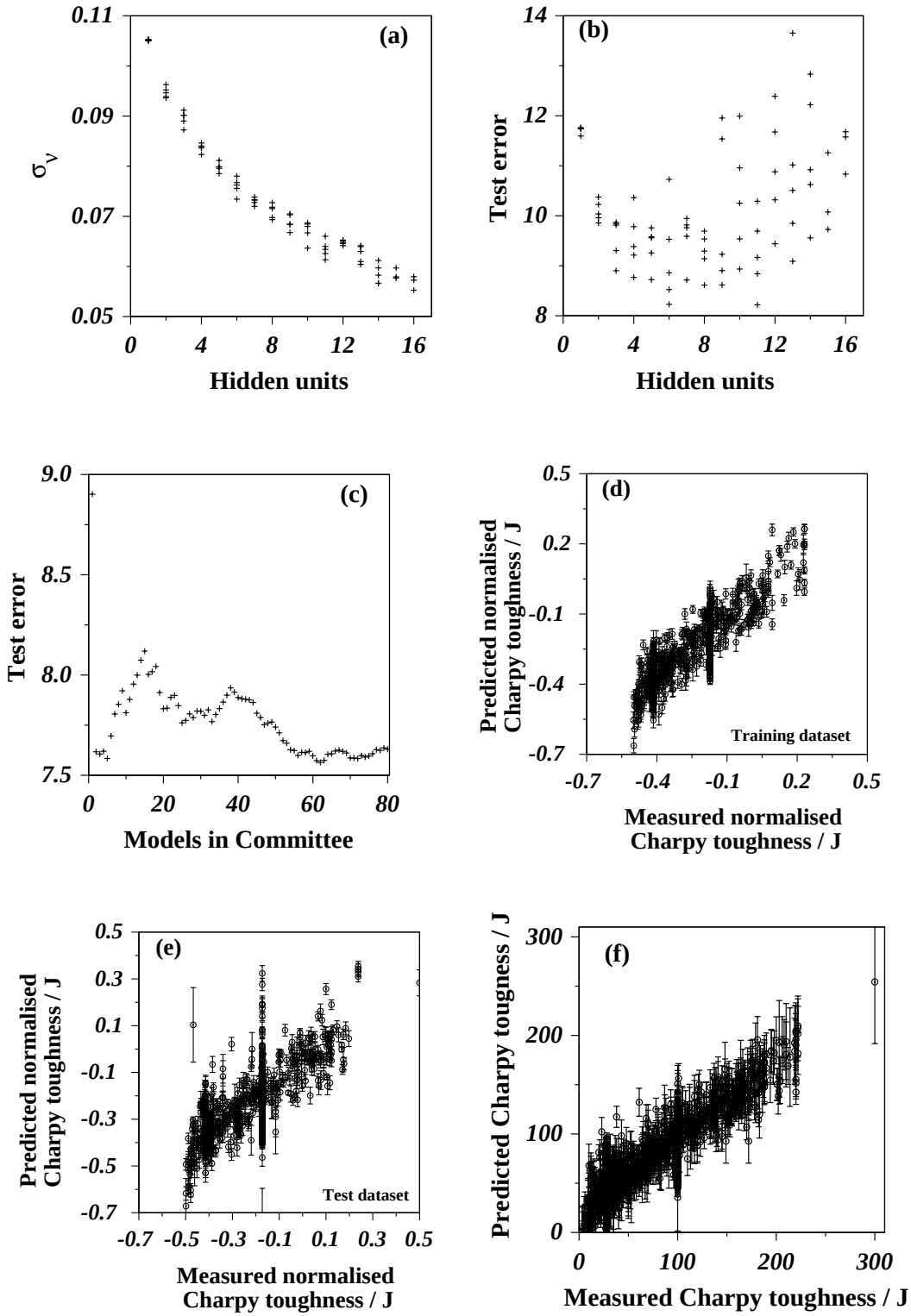

Figure 5.12: Characteristics of the Charpy impact toughness model. σ_ν is the model perceived level of noise in the toughness. (d) and (e) represent the behaviour of the best single model, whereas (f) shows the performance of the optimum committee model on the entire dataset.

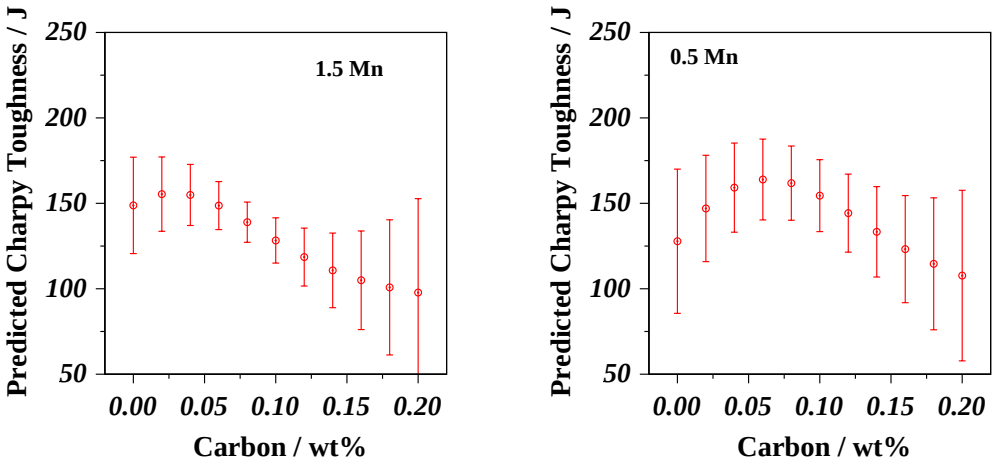

Figure 5.13: Effect of carbon at 1.5 and 0.5 wt% manganese, 0°C, on the Charpy impact energy.

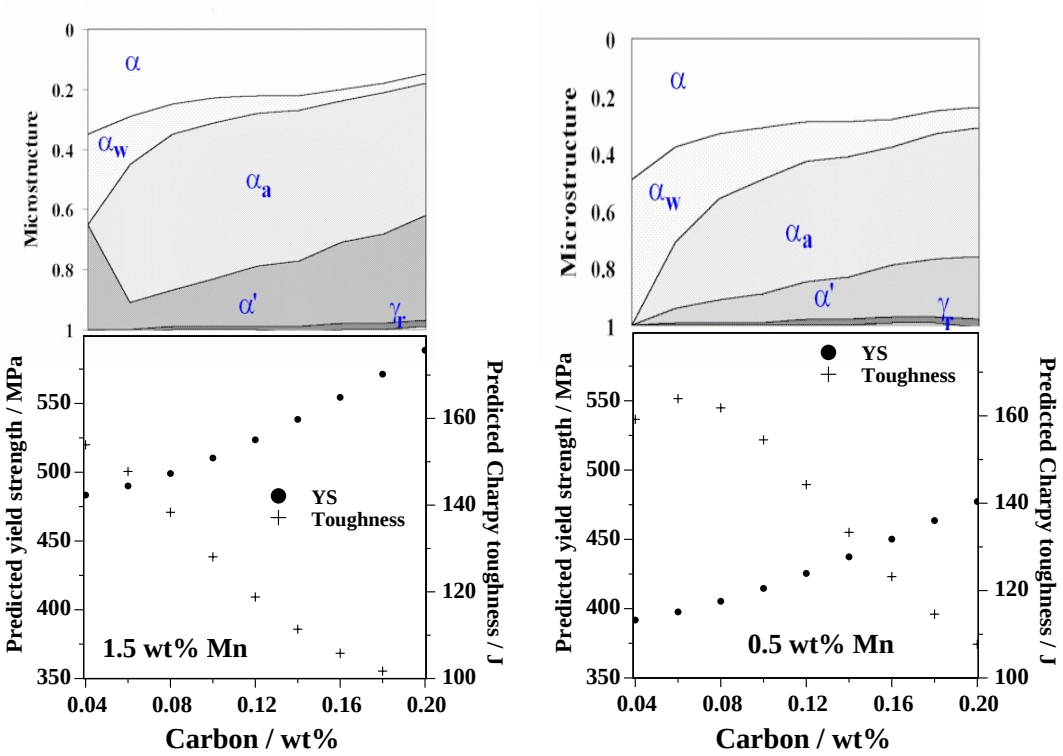

Figure 5.14: Effect of carbon at 1.5 and 0.5 wt% manganese at on yield strength and the calculated microstructural fraction using published physical model [109]. (allotriomorphic ferrite – α, Widmanstätten ferrite – α_w, acicular ferrite + bainite – α_a, martensite – α' and retained austenite – γ_r)

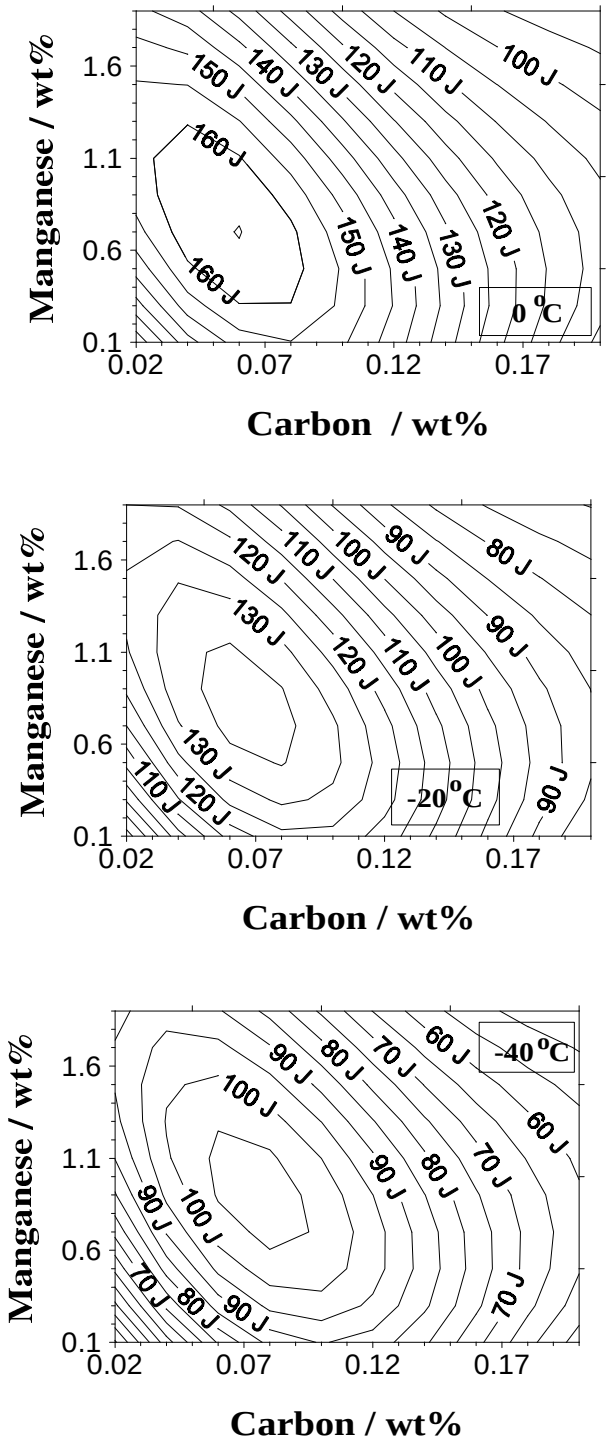

Figure 5.15: Predicted variations in Charpy impact toughness as a function of the carbon and manganese concentrations and the test temperature. The error bars have been omitted for clarity but range from ±10–45 J.

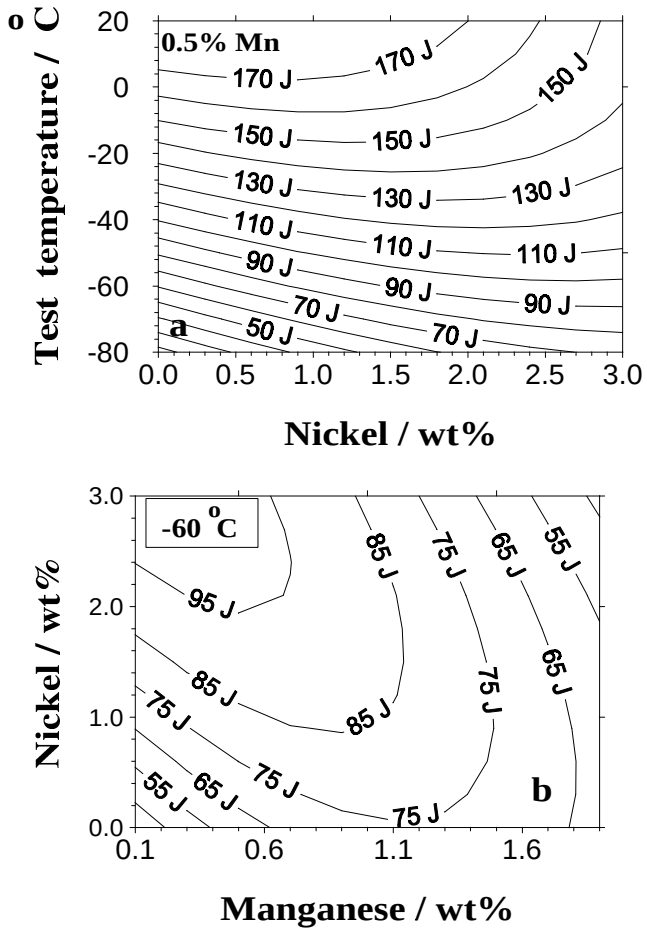

Figure 5.16: The effect of nickel and manganese on the Charpy toughness. (a) Nickel improves the toughness at low temperatures. (b) The optimum concentration of nickel depends on the manganese concentration. The error bars have been omitted for clarity but range from ±10–25 J.

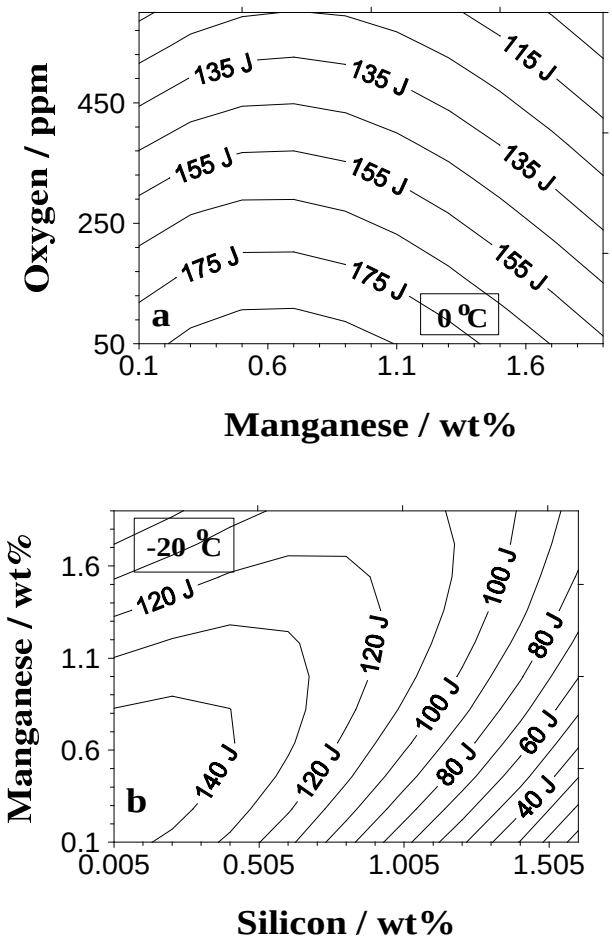

Figure 5.17: (a) The combined effect of manganese and oxygen on the toughness at 0 °C. (b) The combined effect of manganese and silicon on the toughness at -20 °C. The error bars have been omitted for clarity but range from ±10–60 J.

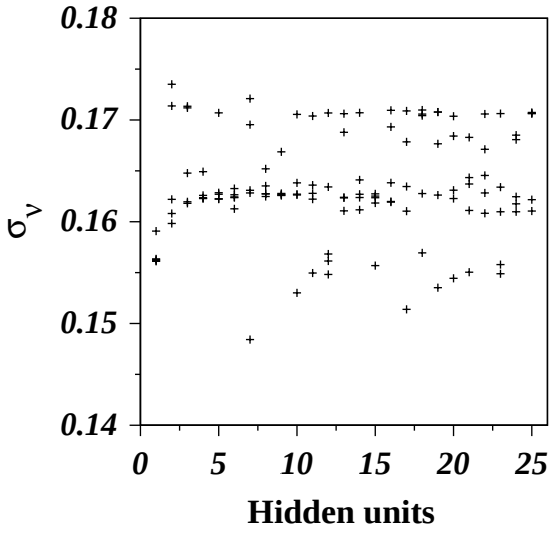

Figure 5.18: Variation in σ_ν as a function of the number of hidden units. Several values are presented for each set of hidden units because the training for each network started with a variety of random seeds.

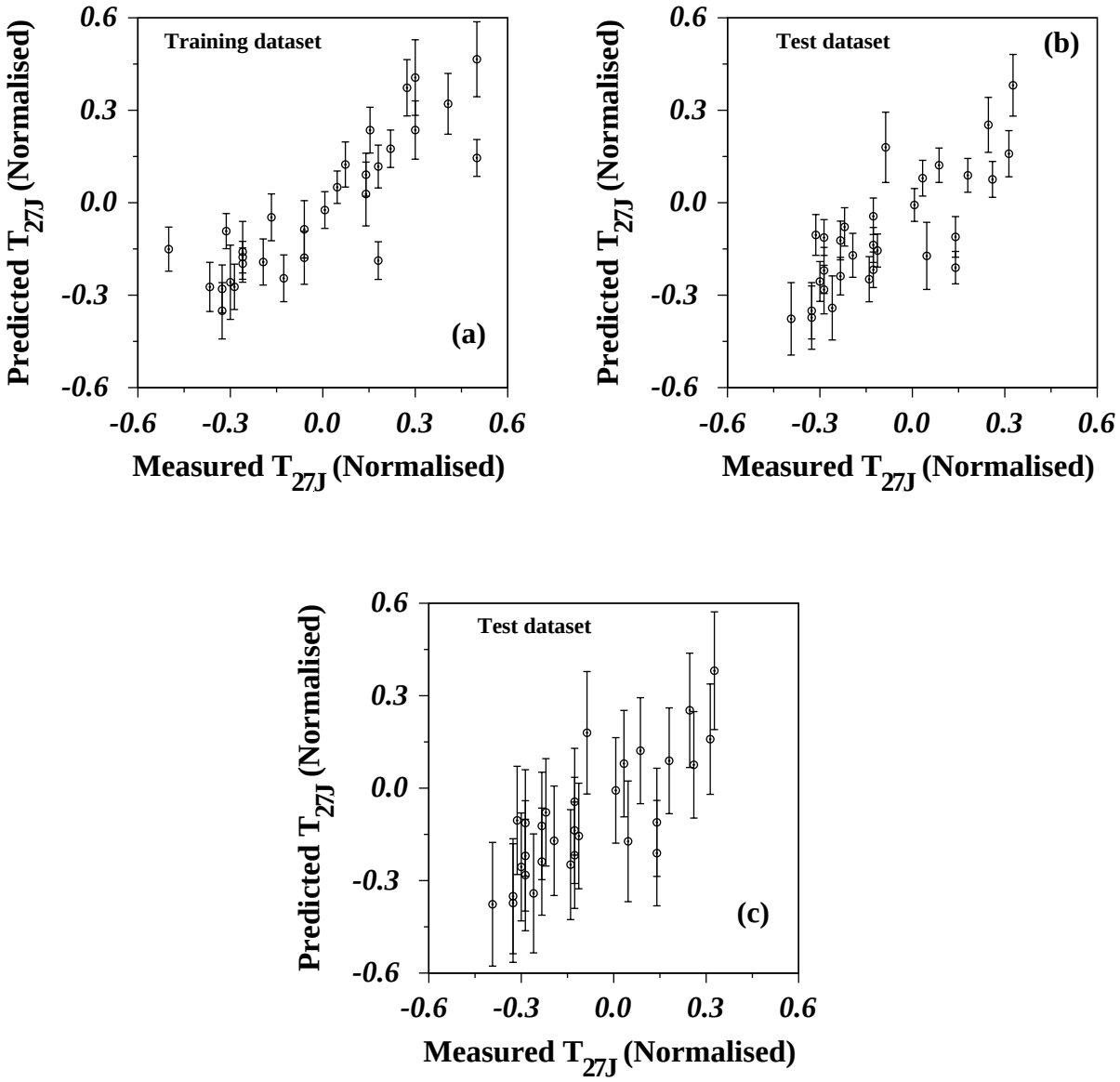

Figure 5.19: Comparison of the predictions made using the best model and measured values of T_{27J}, (a) training data plotted with the fitting error, (b) test data plotted with the fitting error, (c) test data with the error bars representing both the fitting error and σ_ν.

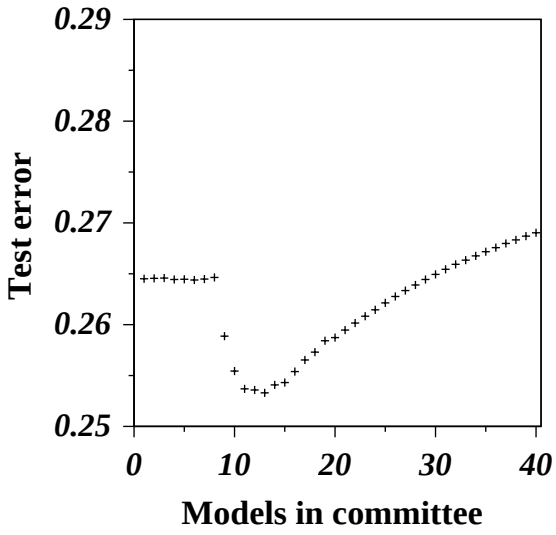

Figure 5.20: Comparison of test error of increasing size of committees.

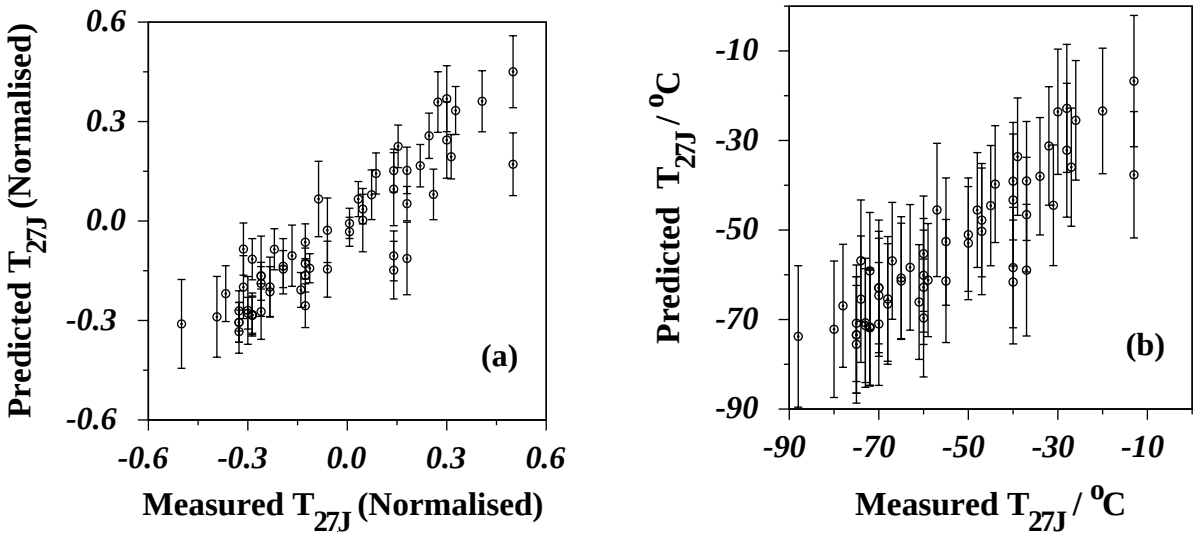

Figure 5.21: Comparison of predicted values and experimental values for the optimum committee using entire dataset a) before unnormalisation, here the error bars contains only the fitting error. b) after unnormalisation, with fitting error and σ_ν.

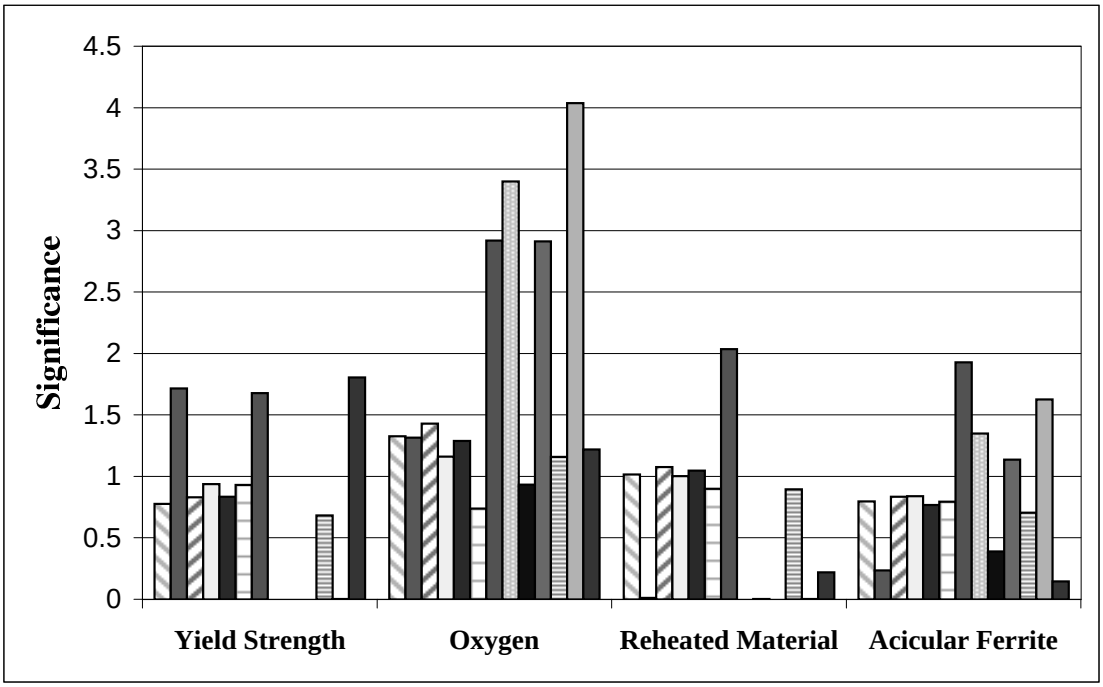

Figure 5.22: Bar chart showing the perceived significance (σ_w) for each input variable. There are thirteen bars plotted per input, corresponding to each of the thirteen members of the optimum committee.

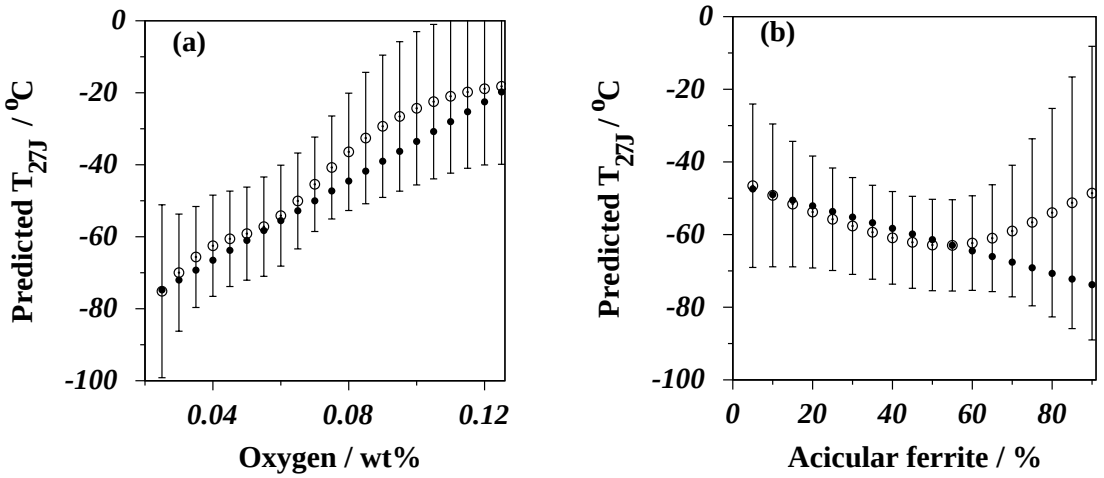

Figure 5.23: Calculations as a function of the oxygen and acicular ferrite contents. In each case, the values of the remaining input variables are as listed in Table 5.6. The open circles with error bars are represent neural network model predictions whereas the filled circles are from equation 5.5.

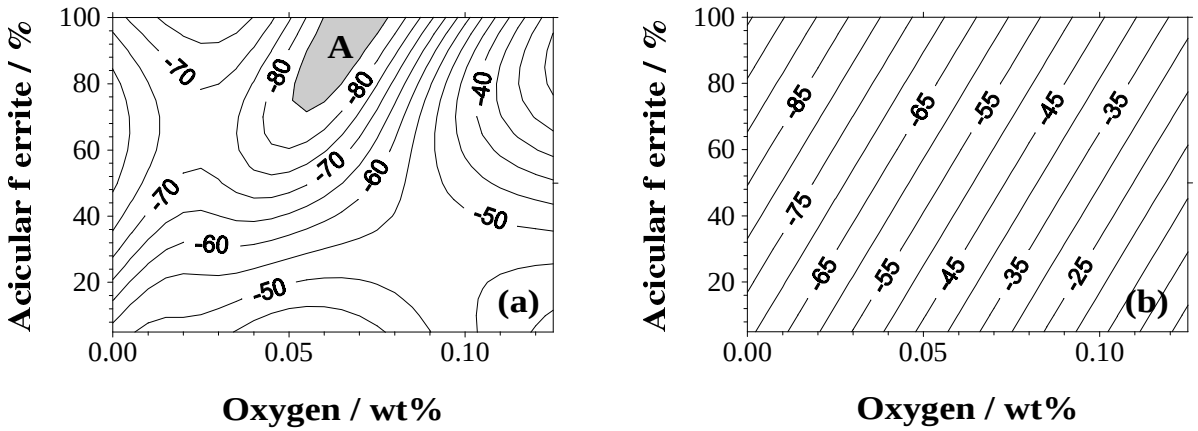

Figure 5.24: Contour plots for calculations made using the following inputs: 510 MPa yield strength and 20% reheated material. The contour lines are expressed in °C, a) neural network predictions, here the error bars have been omitted for clarity but range from ±15–75 °C. The region marked 'A' shows that an optimum value of T_{27J} occurs at finite oxygen concentrations, b) using equation 5.5.

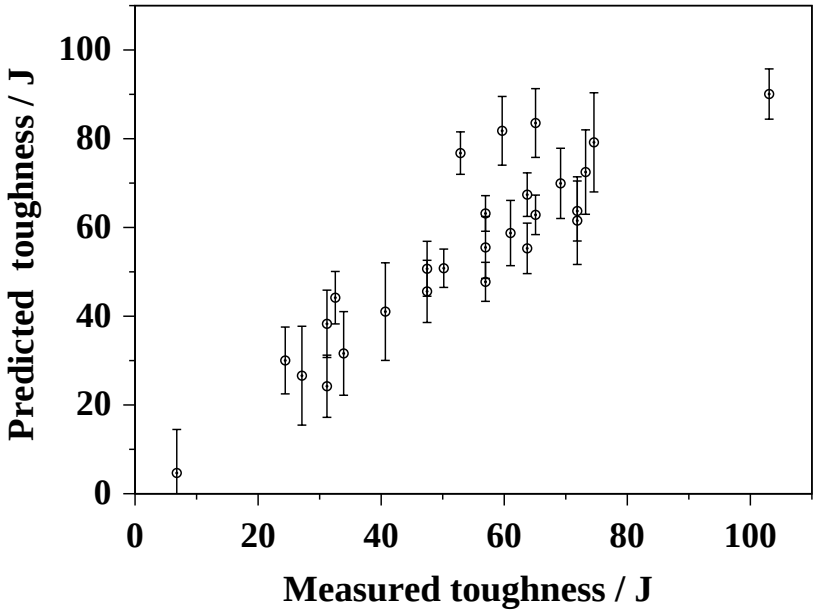

Figure 5.25: Comparison of the predicted and measured values of the Charpy toughness. The predictions are made using the committee of three models.

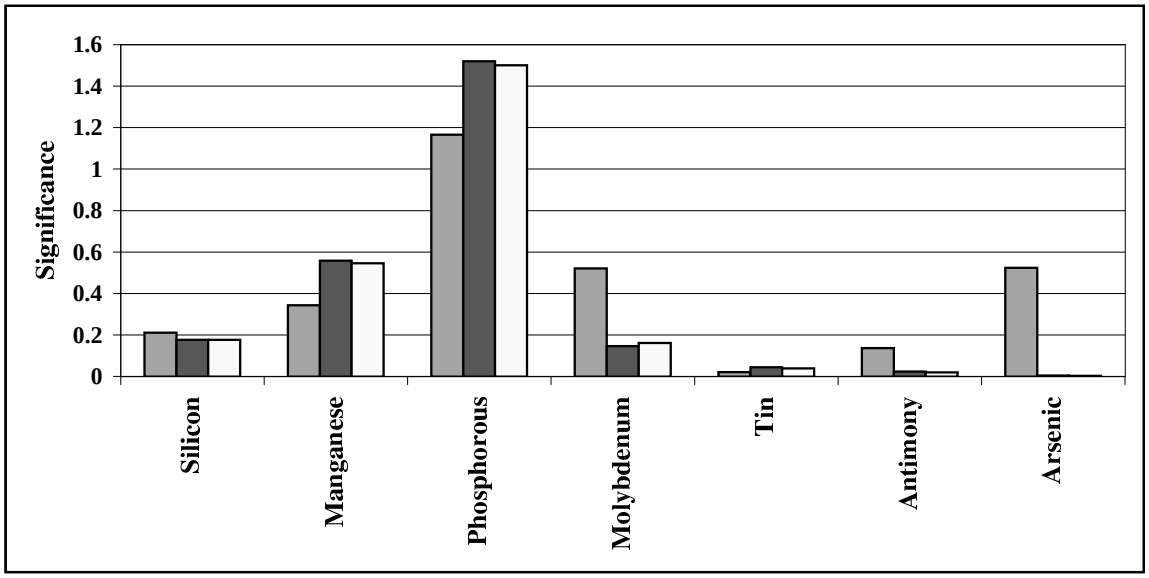

Figure 5.26: The perceived significance σ_w values of three committee models for each of the inputs.

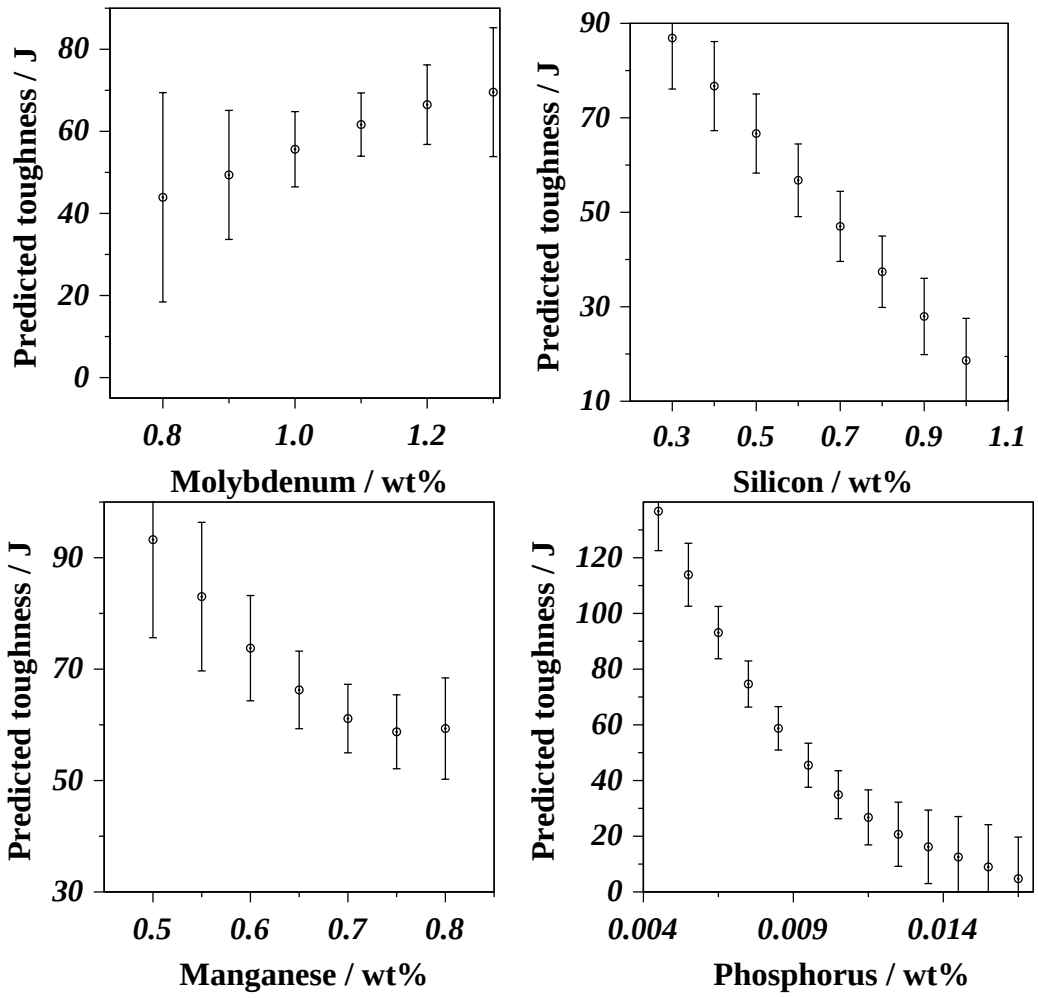

Figure 5.27: Analysing the effects of molybdenum, silicon, manganese and phosphorus on toughness after step aging.

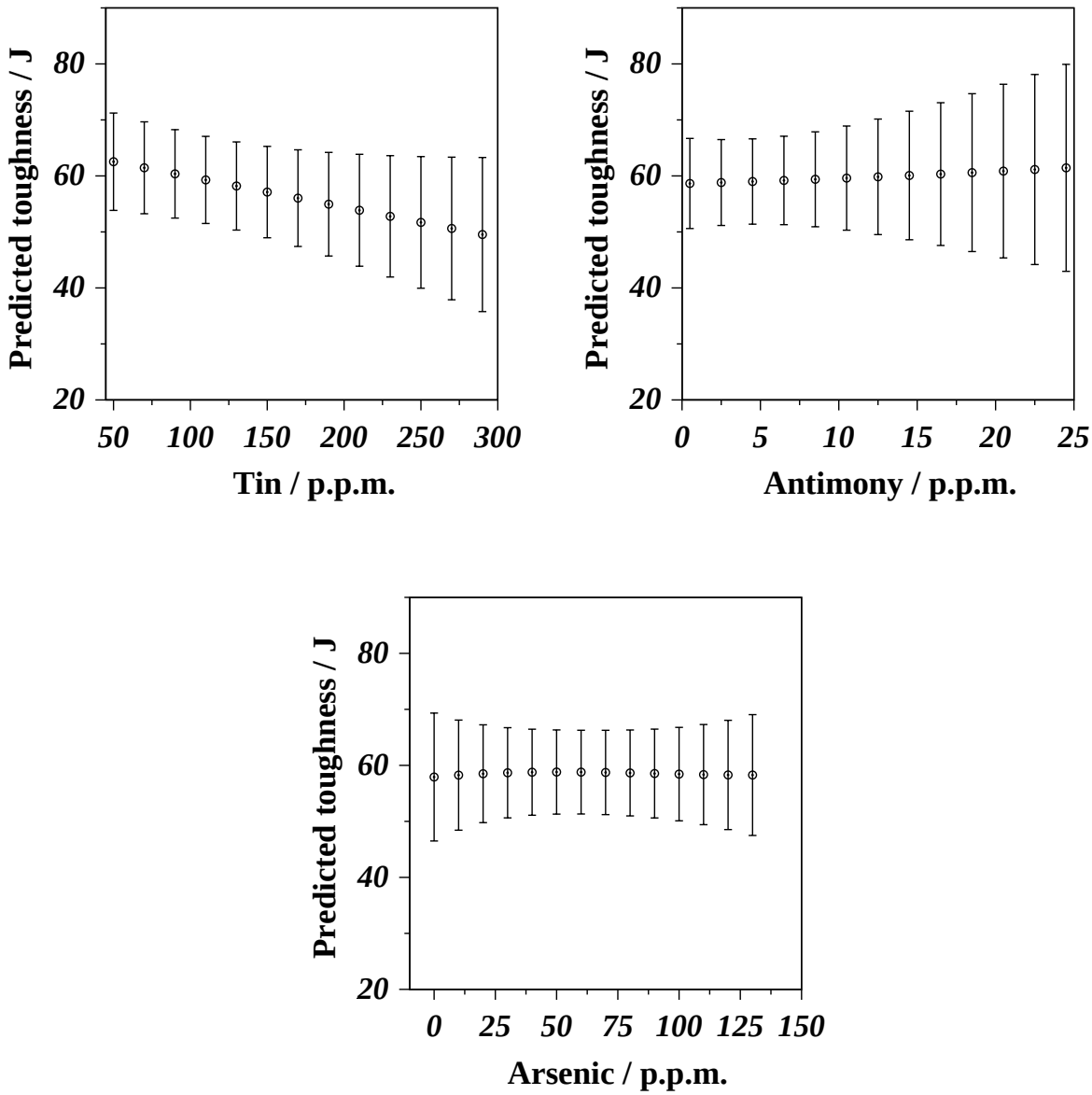

Figure 5.28: The effects of tin, antimony and arsenic on toughness after step aging. 'p.p.m.' corresponds to parts per million.